RSC Applied Interfaces

ROYAL SOCIETY OF CHEMISTRY

PAPER

View Article Online
View Journal | View Issue

Cite this: *RSC Appl. Interfaces*, 2025, **2**, 1838

Hydrogen evolution reaction by Gd-doped transition metal dichalcogenide VSe_2 nanoflowers

Abinash Parida, Banaja Dandasena and Ramakanta Naik *

Received 1st August 2025,
Accepted 22nd September 2025

DOI: 10.1039/d5lf00220f

rsc.li/RSCApplInter

Renewable energy sources, such as hydrogen, are helpful in reducing the dependence on fossil fuels. Electrocatalytic water splitting produces hydrogen, which is a cleaner and more reliable energy source than fossil fuels. The number of exposed active sites in a catalyst considerably affects its catalytic activity. Recently, transition-metal dichalcogenides have been widely investigated for their electrochemical performance. In this context, we prepared Gd-doped VSe_2 nanocomposites $V_{1-x}Gd_xSe_2$ (x = 0, 0.2, and 0.3) using a simple and inexpensive hydrothermal method for the catalytic hydrogen evolution reaction (HER). The prepared sample possessed a nanoflower-like surface morphology with an increase in bandgap from 2.6 to 3.6 eV by Gd doping. The Gd-doped samples showed significantly better electrochemical properties than the pure VSe_2 sample. The highest Gd-doped sample showed the highest electrochemical performance, with an onset potential around 210 mV and a low value of the Tafel slope of around 60 mV per decade, with respect to other samples. This sample also showed a low charge-transfer resistance value of around 1.30 kΩ (calculated from impedance data), which showed good agreement with the HER polarization data and Tafel plot.

1. Introduction

Transition-metal dichalcogenides (TMDs) are suitable for the HER catalysis because of their distinctive layered structures and tunable electrical characteristics. Their catalytic activity is increased by the high electrical conductivity of their 1T metallic phases in particular.[1] These materials are more abundant and lesser expensive than noble metals, which help to overcome the economic issues in the HER catalyst design. In order to catalyze the HER, TMDs need effective hydrogen adsorption on active sites that are mostly found at the edges of their nanosheets. The HER performance is significantly influenced by the interaction between hydrogen atoms and the catalyst surface.[2] The catalytic activity can be greatly increased by altering the electrical architectures of TMDs or engineering them to reveal more active edge sites.[3] Recent studies have improved the fabrication of 2D TMD nanosheets and composites, increasing the efficiencies of photocatalysis and electrocatalysis for hydrogen evolution.[4] These materials have demonstrated promise in photoelectrochemical applications for sustainable hydrogen generation and pure electrochemical HER. Furthermore, to maximize its HER performance, a variety of techniques have been used, including phase engineering, doping, and heterostructure construction.[5] Research has indicated that TMD catalysts have strong stability in practical applications, sustaining catalytic activity for prolonged testing durations.[6] Their cost-effectiveness, stability, and catalytic efficiency make them very appealing for scalable hydrogen generation systems.[7]

Extensive research has been done on TMDs for many years. Because of the distinct crystal and electronic band structure of TMDs, two-dimensional, stacked, thin TMDs have recently attracted a lot of interest in nanoelectronics, optoelectronics, and electrochemical energy storage. Advancements in electrochemical energy storage have resulted in high-performance devices by transforming the electrical structure of TMDs to increase their conductivity. According to recent studies, increasing the conductivity of MoS_2 through a transformation from the 2H phase (semiconducting) to the 1T phase (metallic) can improve its performance in the hydrogen evolution reaction. However, complex chemical treatments are required since these 1T products are thermodynamically unfavorable.[8,9] There is a chance that a TMD material with a comparatively higher electrical conductivity could improve the HER performance. One common multilayer TMD is vanadium diselenide (VSe_2), which has strong electrical conductivity (G = ~1000 S m^{-1} at 300 K) and metallic characteristics.[10]

Traditional fossil fuels, which are rapidly running out and harming the atmosphere, are anticipated to be replaced with

Department of Engineering and Materials Physics, Institute of Chemical Technology-IndianOil Odisha Campus, Bhubaneswar, 751013, India. E-mail: ramakanta.naik@gmail.com

clean, high-energy-density hydrogen fuel produced by electrocatalytic water splitting.[11–14] Currently, platinum (Pt) metal and its associated compounds are thought to be the most effective HER electrocatalysts. However, their nondurability in acidic environments, scarcity and high cost significantly limit their broad usage.[15] Thus, there is an urgent need to design inexpensive, noble-metal-free catalysts with excellent HER performance.[16–18] The most promising substitutes for Pt-based electrocatalysts in recent years have been 2D TMD materials, such as VSe_2,[19,20] VS_2,[21] WTe_2,[22] $ReSe_2$,[23] $MoTe_2$,[24,25] $MoSe_2$,[26,27] and MoS_2,[28–30] due to their distinct layered structure with special chemical and physical characteristics. However, since the majority of HER active sites are frequently found on the visible metallic edges, their activity is restricted by catalytically inert interior planes.[31] As a result, compounds with large exposed active sites in layered structures must be designed.

In the class of TMD materials, the most extensively studied member for electrochemical uses such as energy storage, electrocatalysis, and sensing is vanadium diselenide (VSe_2).[32] Doping TMDs with the right metals can improve their characteristics.[33] The rare earth metal gadolinium (Gd) has unpaired electrons in its f and d orbitals. In addition to providing a large number of reactive sites, the Gd^{3+} ion serves as an electron reservoir to facilitate charge transfer.[34] For example, a maximum surface-to-volume ratio, outstanding catalytic activity, and superior stability are provided by the doping and integration of Gd^{3+} into an electrode.[35] During redox processes, the doping of Gd^{3+} constantly reduces the charge-transfer resistance and enhances the electrochemical conductivity. The electronic structure of VSe_2 is greatly impacted by Gd doping, which results in noticeable alterations to its characteristics. As the Gd doping concentration increases, the bandgap values for Gd-doped VSe_2 also increase, ranging from 2.6 eV to 3.6 eV.[36] This increase in the bandgap is attributed to a complex interplay of charge-carrier localization, modification of the Fermi level, spin–orbit coupling, and alterations in the electronic structure due to the presence of the Gd dopant. Gd has a larger ionic radius than the constituent elements of VSe_2, V and Se, which results in structural modifications when it is added to VSe_2. The size mismatch results in local lattice distortions in the VSe_2 crystal structure. In our previous study, we investigated the optical nonlinearity for the optoelectronics applications of Gd-doped VSe_2 nanocomposites.[36]

In the present study, we prepared Gd-doped VSe_2 nanocomposites through the hydrothermal synthesis method. The electrochemical characteristics of the samples were investigated through several measurements. In addition to their electrochemical performance, different structural, optical, and morphological characteristics were also investigated through different characterizations. The phase and crystallinity of the material were probed using an X-ray diffractometer (XRD). FESEM and TEM were used for morphological characterization. Different planes with interplanar spacing were identified through a high-resolution transmission electron microscope (HRTEM). Selected area electron diffraction (SAED) was used to locate various planes. The reflectance was measured using UV-visible spectroscopy, which helped in the mathematical computation of the bandgap energy.

2. Experimental procedure

2.1. Chemicals for the study

In the synthesis process, we used chemical salts, namely ammonium metavanadate (NH_4VO_3, 98%, Fisher Scientific), gadolinium(III) nitrate hexahydrate [$Gd(NO_3)_3{\cdot}6H_2O$] (99.99%, Sigma Aldrich), oxalic acid ($C_2H_2O_4{\cdot}2H_2O$), and selenium powder (Alfa Aesar, 99.99%) for preparing VSe_2 and the Gd-doped VSe_2 samples.

2.2. Sample preparation

The sources of selenium, vanadium, and gadolinium in these samples were selenium powder, NH_4VO_3, and [$Gd(NO_3)_3{\cdot}6H_2O$], respectively. The flower-like VSe_2 sample was produced by the standard hydrothermal process. The stoichiometric amounts of 1 mmol of NH_4VO_3, 2 mmol of Se in powder form, and 9.5 mmol of $C_2H_2O_4{\cdot}2H_2O$ were combined with 40 mL DI water inside a beaker. After the solution was ready, it underwent an hour of stirring. After this step, the prepared solution was stored inside a 50 mL autoclave, then heated to 200 °C for 24 hours. Following three rounds of washing in ethanol and DI water, the synthesized product was vacuum-dried for 24 hours at 60 °C. The same process was followed twice for doping Gd (0.2, 0.3). The prepared samples described herein were named VS for VSe_2, GVS-1 for 0.2 mmol-Gd doping, and GVS-2 for 0.3 mmol-Gd doping. The nanocomposites were then used for different characterizations. The complete procedure for synthesizing the nanocomposites is illustrated in Fig. 1.

2.3. Characterizations

After the preparation of the nanocomposites, their morphological, optical, and structural alterations were examined using a variety of procedures. XRD data was collected by a Bruker D8 Advance machine. Cu K_α (wavelength = 0.154 nm) was the X-ray source, which was operated at 30 kV operating voltage and 40 mA current. The XRD measurement scan was from 10° to 70°, with a step size of 0.02° and scan rate of 0.5° per step. The surface structure was imaged through JEOL-JSM-7610F operating at 15 kV voltage (electron beam) with a 9×10^{-5} Torr vacuum. The high-resolution images of the samples were taken with a JEOL TEM-2100 Plus instrument. The elemental content of the samples was examined using energy-dispersive X-ray spectroscopy (EDS). To discuss the optical data, the reflectance spectra ranging from 280–750 nm were acquired using a JASCO V-770 UV-visible spectrophotometer.

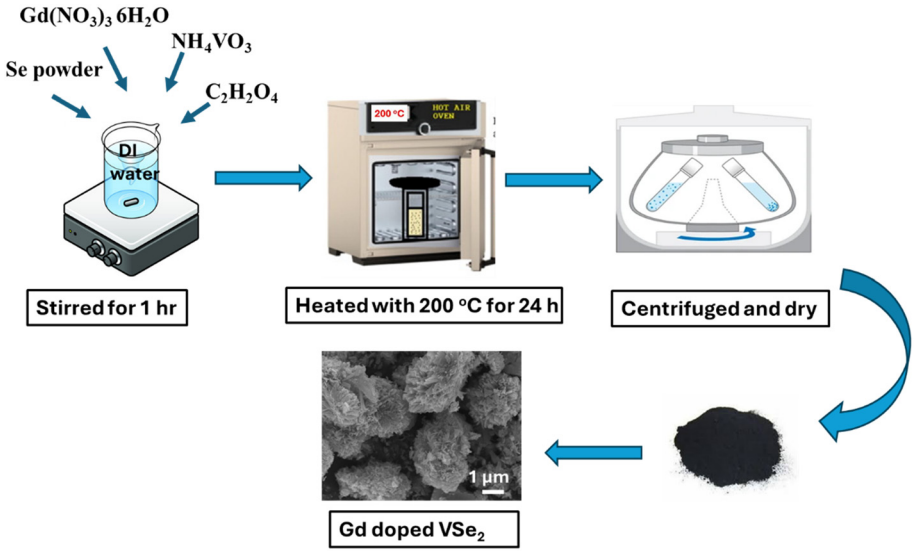

Fig. 1 Complete synthesis process of the Gd-doped VSe_2 nanocomposites.

2.4. Electrochemical measurement

The electrochemistry experiments were performed using Autolab (AUT87691) at ambient temperature. The three-electrode system was configured with Ag/AgCl as the reference electrode, platinum as the counter electrode, & glassy carbon as the working electrode. Potassium hydroxide (KOH, 1 M) solution was used as the electrolyte in all the tests. The equation $E_{RHE} = E_{Ag/AgCl} + 0.1976 + 0.056$ pH is used to report all the potentials in the current study. This is due to the reversible hydrogen electrode RHE. For preparing the catalyst ink, 70 wt% of the prepared materials (VS, GVS-1, and GVS-2), 20% conductive carbon black, and 10% PVDF as a binder were ground well in a mortar and pestle. A few drops of *N*-methyl pyrrolidone (NMP) were added and stirred well to prepare a homogeneous slurry. Using the drop-casting technique, the slurry was coated onto the glassy carbon electrode and dried in an oven at 60 °C overnight. For all the electrochemical experiments, 1 M KOH solution was utilized as an electrolyte solution. The electrochemical characteristics of the studied samples were observed by cyclic voltammetry (CV), linear sweep voltammetry (LSV) measurements and electrochemical impedance spectroscopy (EIS).

3. Results

3.1. XRD study

A thorough understanding of the structural characteristics of the material can be gained from XRD analysis. The XRD patterns of both pure and Gd-doped VSe_2 are shown in Fig. 2(a). There are eight prominent peaks in the XRD pattern, which are easily indexed to the standard JCPDS data of VSe_2 (JCPDS card no. 01-89-1641). The reflection peaks are located at 2Θ values of 14.6°, 29.2°, 30.8°, 34.1°, 42.8°, 54.6°, 60.7°, and 66.09°. These values correspond to the (0 0 1), (0 0 2), (1 0 0), (0 1 1), (1 0 2), (1 1 0), (0 0 4), and (2 0 1) planes.[37]

A close examination of the GVS-1 and GVS-2 patterns shows extra weak reflections that are absent from the pristine sample and additional VSe_2 peaks. These additional peaks can be attributed to the V_3Se_4 phase (ICDD card no. 00-017-

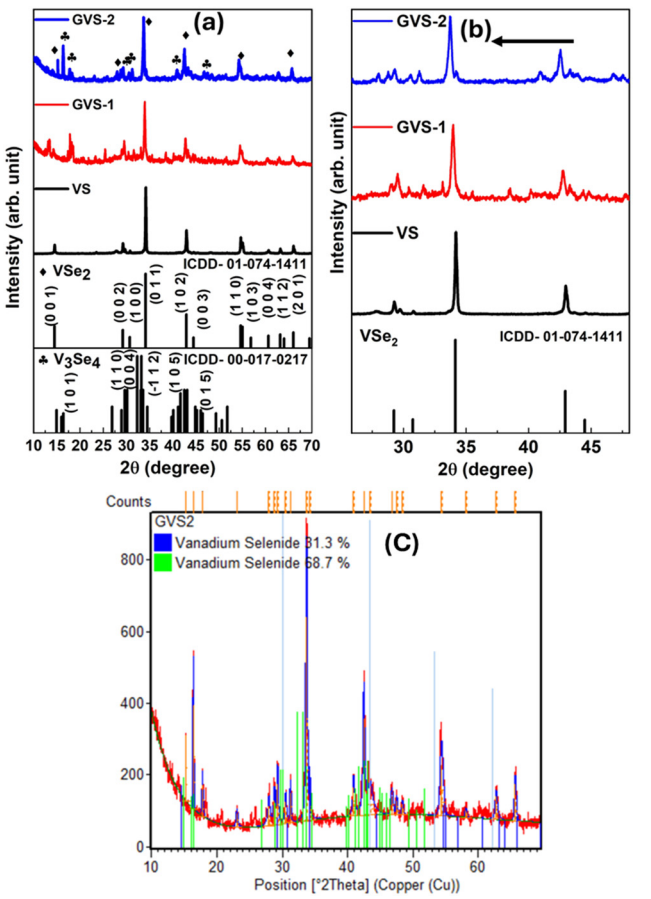

Fig. 2 (a) XRD pattern, (b) shifts in the XRD peaks due to doping, and (c) Rietveld refinement of the GVS-2 sample.

0217). The peaks shifted to lower angles following gadolinium (Gd) doping, as shown in Fig. 2(b). This result could be because Gd has a larger ionic radius than the elemental components, vanadium (V) and selenium (Se), in VSe_2.[38] Local lattice distortions can result from the atomic size mismatch when Gd is added to the VSe_2 crystal structure. The shift in the XRD peaks was a result of this alteration in the interatomic gap. The peak shift to lower angles in this instance was caused by doping, which caused the lattice to expand and enhanced the interplanar spacing (*d*-spacing). Rietveld refinement was carried out using the X'pert Highscore Plus (XHP) software and involved accounting for both the VSe_2 and V_3Se_4 phases in order to validate this observation, as shown in Fig. 2(c). The scale factors and profile parameters were calibrated to a reference with a standard profile. The quality of fit for the experimental data was evaluated using reliability parameters, such as the weighted profile factor ($R_{w.p}$), expected factor (R_{exp}), and goodness-of-fit (χ^2); the ratio of $R_{w.p.}$-to-R_{exp} is known as the goodness-of-fit (χ^2).[39] The findings of the different *R* factors of the Rietveld refinement for the present sample were as follows: $R_{w.p.}$ = 12.7, R_{exp} = 9.1, and the goodness-of-fit χ^2 = 1.3. The coexistence of two phases in the Gd-doped samples was confirmed by the refinement, which displays a good fit between the estimated and observed profiles. There might be a partial reduction of VSe_2 that occurred under the impact of Gd doping during hydrothermal synthesis, which is responsible for the emergence of the V_3Se_4 phase. The inclusion of Gd^{3+} altered the chemical environment, resulting in V-rich domains that promoted the formation of V_3Se_4.

3.2. FESEM, EDS, and TEM analyses

The FESEM analysis shows the difference in the morphology of the samples prepared with different amounts of vanadium and gadolinium. Fig. 3(a) displays the shape of pure VSe_2. The images show that VSe_2, which is hydrothermally produced, forms several flower-like structures; thin sheets build up to form a structure that resembles a flower. Specifically, these microflowers are structurally similar to marigold flowers. The produced samples that exhibit the morphology of nanoflowers further accumulated to form microsphere-like structures that are uniformly distributed all over the sample and range in size from 1.7 to 2.5 μm. Fig. 3(b) and (c) shows the Gd-doped samples, GVS-1 and GVS-2, at the micrometer scale. The nanoflower-like morphology is due to the intrinsic layered structure of VSe_2 that appears as a sheet-like crystal growth during the hydrothermal synthesis. These nanosheets self-assembled into clusters that resemble three-dimensional flowers in order to reduce surface energy. Gd doping affected this process by acting as a structural modifier and nucleation center. The inclusion of Gd^{3+} ions caused localized lattice strain and changed the surface charge density, facilitating increased nucleation sites and suppressing uncontrolled lateral sheet growth. The flower-like VSe_2 structures appear similar to previously described "nanoflower" morphologies in VSe_2-based systems. However, the formation methods and material chemistry differ. In hybrid systems like VSe_2–$CoSe_2$, a flower morphology has been determined by the co-nucleation and relative fraction of two unique selenide phases generated during one-pot synthesis.[40] Phase composition also influences morphology. In contrast, the nanoflower architecture in our study originated from the self-assembly of the ultra-thin VSe_2 nanosheets, whose nucleation and lateral growth were modified by Gd substitution. The EDS spectra for the synthesized samples are displayed in Fig. 4. These spectra demonstrate the presence of the material's constituent elements. The doped composites exhibit a Gd peak, while the bare VSe_2 composition exhibits peaks of elemental V and Se. Table 1 shows the EDX profile indicating the percentage of the constituent elements in the prepared samples. From that table, the observed Gd-dopant concentration agreed well with the expected values.

HR-TEM and SAED analysis can be used to understand crystalline behavior and particle size. The TEM image of the VS sample shows nanosheets arranged like flowers, as shown in Fig. 5(a). The lattice spacing value was determined from the HRTEM images and the matching lattice plane, as shown in Fig. 5(b). The spacing values for the (011) and (101) lattice planes were determined to be roughly 0.26 and 0.21 nm, respectively. These findings match the XRD data from the prepared sample. The SAED patterns in Fig. 5(c) show the crystallinity of the material. Specific ring patterns composed of bright spots can be seen in the SAED image, enabling identification of the crystalline characteristics. Structural parameters, which incorporate the XRD, SAED, and HRTEM findings, indicate that all of the results are consistent and in agreement.

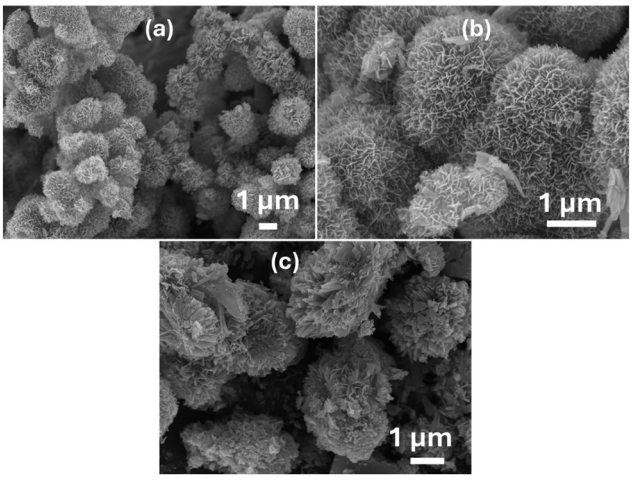

Fig. 3 FESEM images of (a) VS, (b) GVS-1, and (c) GVS-2 at the micrometer range.

3.3. XPS study

The aim of the XPS analysis was to analyse the oxidation states of the components in the prepared samples. The

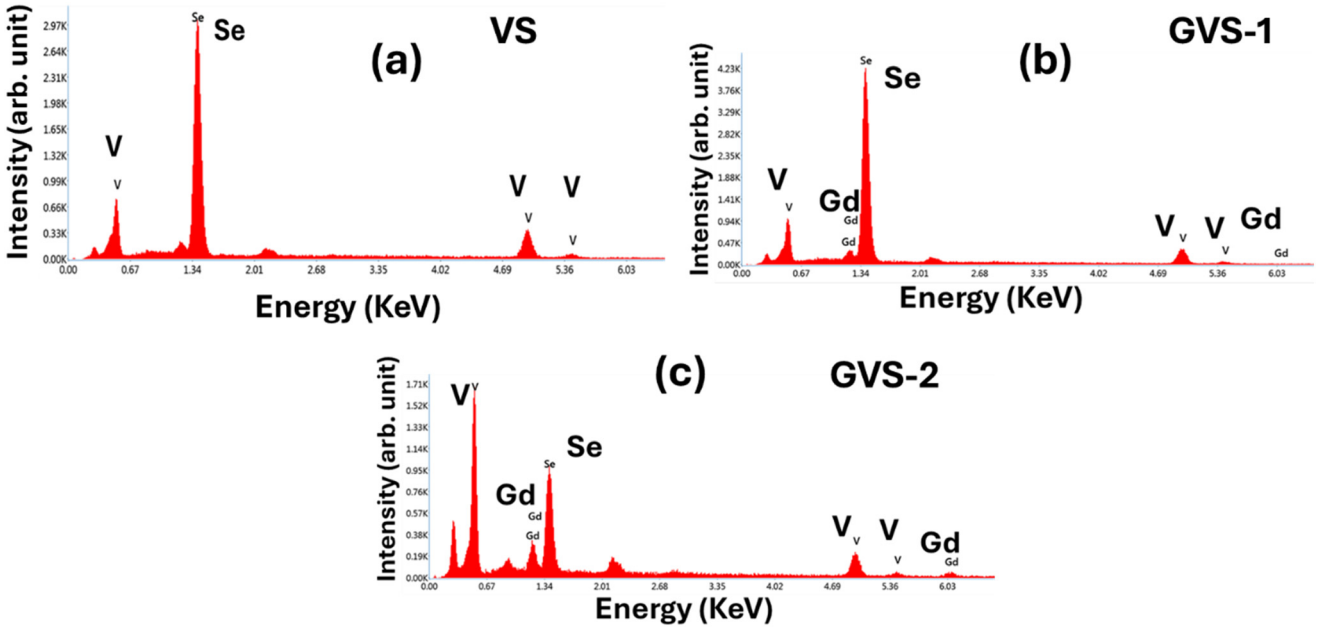

Fig. 4 EDS results of the (a) VS, (b) GVS-1, and (c) GVS-2 samples.

Table 1 EDX compositional percentage of the constituent elements in the prepared samples

	VS		GVS-1		GVS-2	
Samples	Cal. at%	Obs. at%	Cal. at%	Obs. at%	Cal. at%	Obs. at%
V	33.33	31.34	26.64	26.72	23.31	25.21
Gd	0	0	6.66	6.24	9.99	9.75
Se	66.67	68.66	66.67	67.04	66.67	65.04
Total	**100**	**100**	**100**	**100**	**100**	**100**

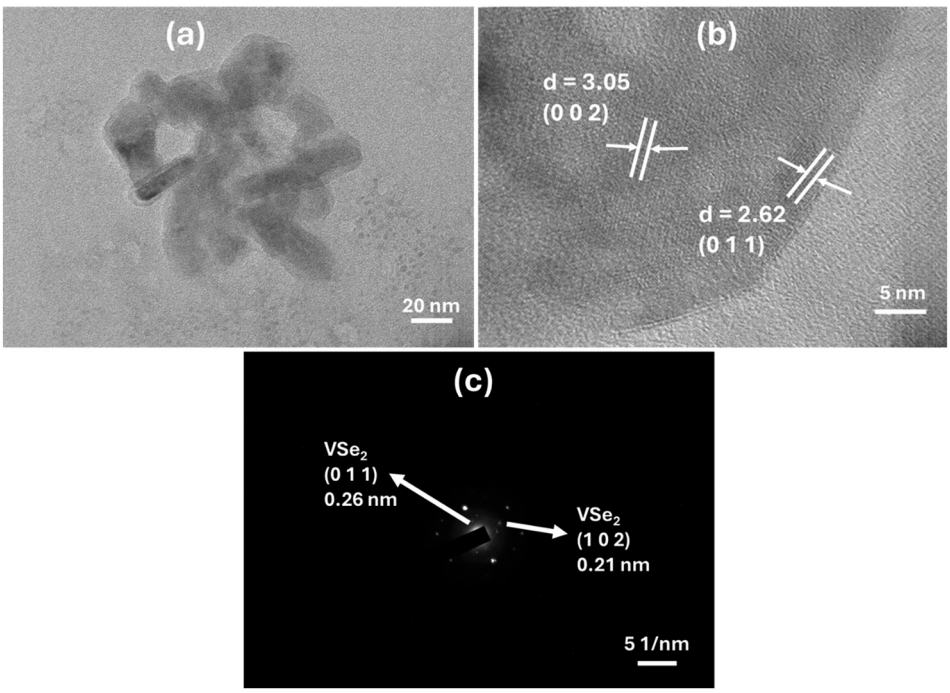

Fig. 5 (a) TEM and (b) HRTEM images and the (c) SAED pattern of the GVS-2 composite.

constituent elements and binding states of a material's surface can be identified by using XPS, a surface analysis technique, which was performed on the GVS-2 sample. This study was carried out by examining changes in the core-level energies of the element. The XPS spectra of V-2p, Gd-3d, and Se-3d are displayed in Fig. 6. As seen in Fig. 6(a), the prepared nanomaterial exhibits two prominent peaks, V $2p_{3/2}$ and V $2p_{1/2}$, at binding energies of 517 and 524.5 eV, respectively. A peak at roughly 517 eV indicates the presence of vanadium's V^{4+}.[41] The +3 oxidation state is responsible for the Gd peaks at 143 and 148.7 eV, as illustrated in Fig. 6(b).[42] Furthermore, Fig. 6(c) displays the XPS analysis of Se 3d. The two different peaks in the spectra, Se $3d_{5/2}$ at 55 eV and Se $3d_{3/2}$ at 56.3 eV, are caused by the −2 oxidation state of selenium.[43] The presence of every compositional element is depicted in the survey scan in Fig. 6(d). The carbon peak at 285 eV was used for standardizing the elemental peaks. These results show that the synthesis of the Gd-doped VSe_2 composite samples was successful.

3.4. Optical study

Fig. 7(a) shows the reflectance spectra for the synthesized VS and GVS samples at wavelengths between 280 and 750 nm. By moving an electron between the valence and conduction band in semiconducting materials, the energy differential between the higher and lower energy states increases. As Gd doping increased, there was a movement of the fundamental absorption edge toward lower wavelengths. The intensity in the reflectance spectra increased with increasing Gd doping, and was at a maximum for the GVS-2 sample. The material's bandgap value was calculated using the Kubelka–Munk method.[44] The following is the expression corresponding to this equation:[45]

$$\frac{k}{s} = \frac{(1-R_\infty)^2}{2R_\infty} \equiv F(R_\infty) \quad (1)$$

Here, $F(R)$ denotes the Kubelka–Munk function and R_∞ is the diffuse reflectance. The optical bandgap values and the Tauc equation are related to the absorption coefficient by the formula:

$$\alpha h\nu = A(h\nu - E_g)^p \quad (2)$$

In the case of perfect diffuse scattering of the incoming light, the absorption coefficient is $k = 2\alpha$. Under these conditions, the scattering coefficients "s" = constant. Consequently, 'k' and $F(R)$ are proportional to each other. The expression can be obtained using eqn (2) as:

$$[F(R_\infty)h\nu]^2 = A(h\nu - E_g) \quad (3)$$

The calculated bandgaps are illustrated in Fig. 7(b–d). Compared to the undoped VS sample, the sample with a

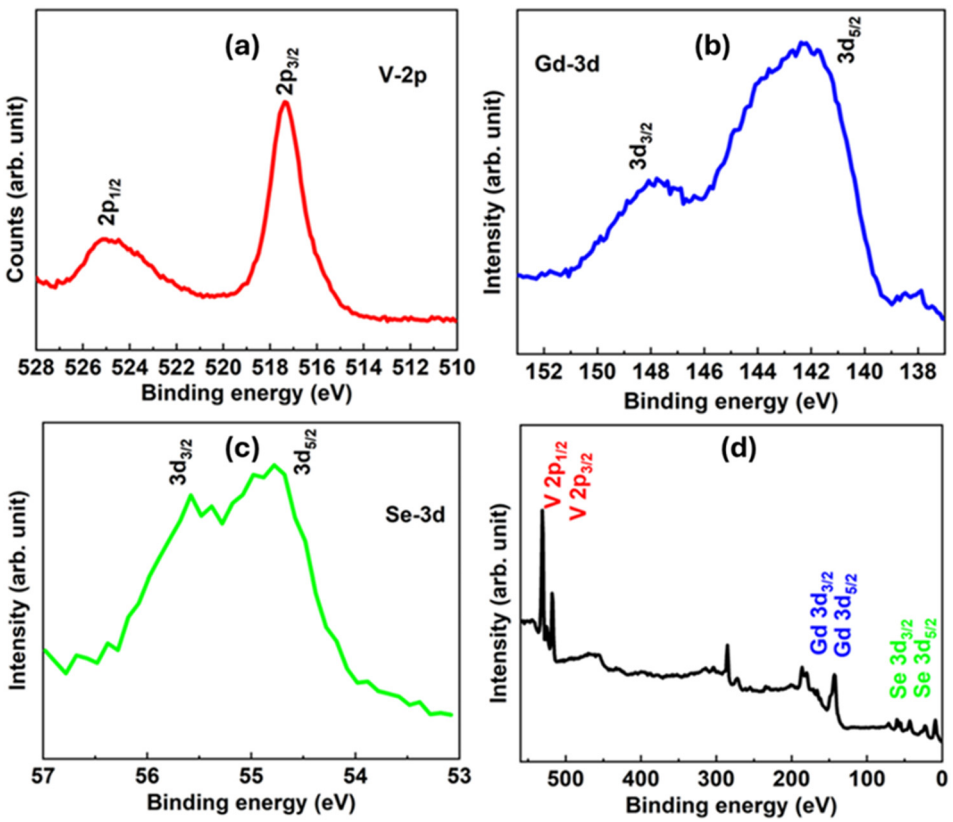

Fig. 6 XPS survey spectra of (a) GVS-2. (b) V 2p, (c) Gd 3d, and (d) Se 3d core spectra of the GVS-2 sample.

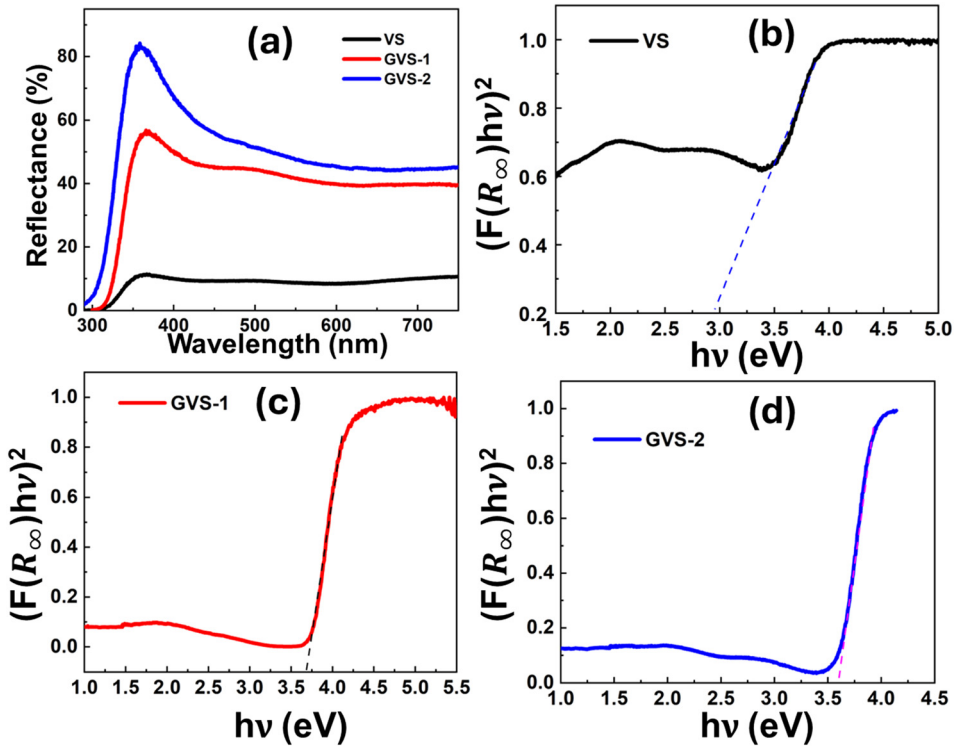

Fig. 7 (a) Reflectance curve of $V_{1-x}Gd_xSe_2$. Calculation of the bandgap value of the (b) VS, (c) GVS-1, and (d) GVS-2 samples.

higher Gd-doping content exhibited a greater bandgap. Based on an estimate, the VSe_2 bandgap was 2.6 eV, and when the amount of Gd doping increased, it increased to 3.6 eV for the GVS-1 sample, and 3.69 eV for the GVS-2 sample. The complicated interactions among spin–orbit coupling, charge-carrier localization, Fermi level change, and dopant (Gd)-induced charges in the electronic structure are responsible for an enhancement in the bandgap. All these characteristics can help to increase the electronic gap between the valence and conduction band of a doped sample.

3.5. Electrocatalytic analysis

At room temperature, we used LSV with a 1 mV s^{-1} scan rate to assess the electrocatalytic characteristics of VSe_2 and the Gd-doped VSe_2 nanocomposite in a 1 M KOH solution. In Fig. 8(a), the polarization curves are displayed. The GVS-2 electrocatalyst had the highest HER catalytic response. It had a 210 mV onset potential, indicating a strong interface interaction and the potential for further activity development. The overpotential of VS was higher in comparison with the GVS samples. The cathodic current increased with a larger negative potential because there was lower electrocatalytic conversion of the proton to H_2. As a result, there was comparatively lower hydrogen evolution activity. It is noteworthy that more catalytic activity can be attributed to the Gd-doped VSe_2. Consequently, we believe that there are unique opportunities to improve the catalytic activity of the VSe_2 material.

The polarization curves were used to obtain the Tafel slope, which can be used for studying the reaction process and kinetics of hydrogen evolution.[46,47] The Tafel slope was estimated from the Tafel relation,

$$\eta = b\log(j) + a \quad (4)$$

where, j = current density, η = overpotential, and b = Tafel slope.[48] Fig. 8(b) illustrates the Tafel slope of the different electrocatalysts. GVS-2 had 60 mV per decade as its Tafel slope. Since this value was significantly lower than that found for the GVS-1 and VS samples, it suggests that the highest Gd-doped sample increased the HER catalytic activity.

To understand the interfacial processes of the GVS compound, the kinetics of HER must be investigated. Understanding how the cathodic H_2 evolution reaction takes place at the electrodes can be assisted by the well-known finding from Conway *et al.* on the involvement of chemisorbed hydrogen.[49,50] In acidic electrolytes, the HER usually consists of three primary stages for converting H^+ to H_2. The three stages are the Tafel reaction, Volmer reaction, and the Heyrovsky reaction. Generally, in the preliminary stage, adsorbed hydrogen intermediates are formed through the interaction of hydrogen ions and electrons. This step is known as the discharge stage or the Volmer step. Furthermore, the second and third steps involve desorption; these are the Heyrovsky reaction and the Tafel reaction, respectively.

The charge-transfer mechanisms of the different electrocatalysts were studied by EIS in order to better

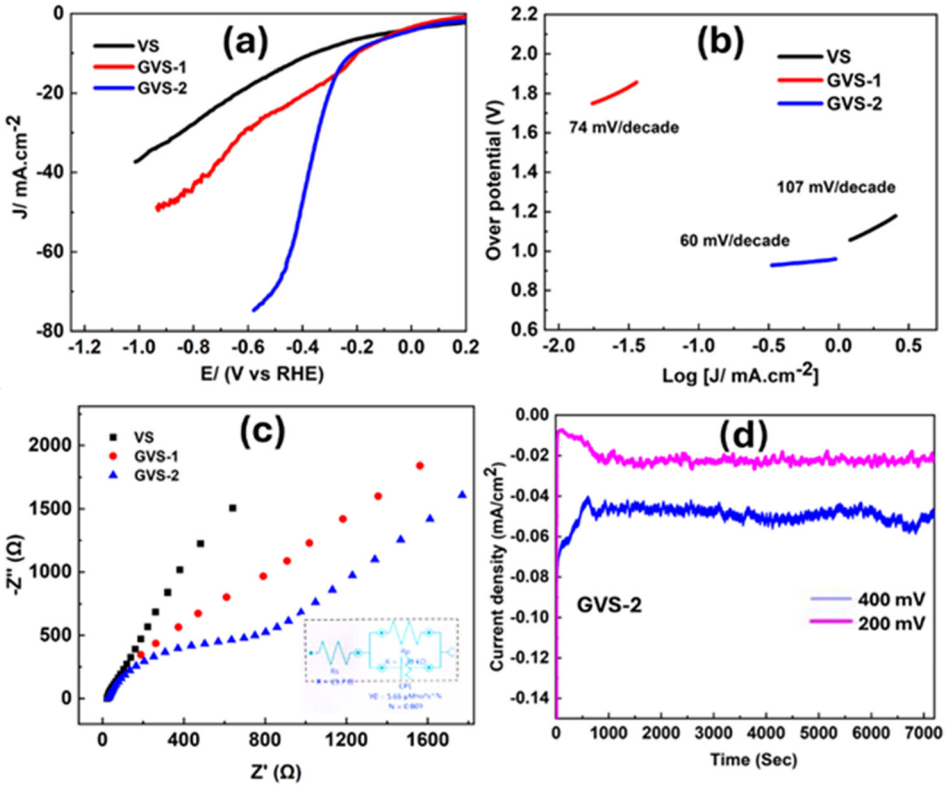

Fig. 8 (a) HER polarization data, (b) calculated Tafel plots, and (c) Nyquist plots of VS, GVS-1, and GVS-2 with circuit diagram as inset. (d) Chronoamperometry plot of the GVS-2 sample.

investigate the connection between the electrocatalyst's active surfaces and catalytic HER activity.[51–53] The resulting Nyquist plot of the VS, GVS-1, and GVS-2 electrocatalysts is displayed in Fig. 8(c). The charge-transfer resistance (R_{ct}) of the electrocatalysts reflects the faradic kinetics of the HER catalytic reaction at the interface. The calculations used a basic Randles-type equivalent circuit that best suited the experimental data.[54] The GVS-2 sample with a higher Gd doped-concentration had a good fit among all the three samples, and the GVS-2 sample had an R_{ct} value of around 1.30 kΩ. This value indicates that GVS-2 is a low-resistance material, which suggests that there was good electrical communication between the two catalytic edges. As a result, the GVS-2 material possessed the highest conductivity. This result is consistent with the polarization measurements, where GVS-2 showed the highest HER performance compared to the other samples. Chronoamperometry was used to investigate the long-term stability and related capacity of the GVS-2 sample for continuously catalyzing the production of H_2. This quasi-electrolysis procedure was carried out in 1 M KOH solution at two constant potentials of 200 mV and 400 mV, as shown in Fig. 8(d). After 2 hours of continuous operation, the H_2 evolution could continue at a constant current density, indicating that the prepared GVS-2 sample had a high stability.

CV is one important electrochemical method for distinguishing between pseudo-capacitance and an electrochemical double-layer capacitor (EDLC).[55] As shown in Fig. 9(a–c), the CVs of VS, GVS-1, and GVS-2 in the aqueous state were determined in a 1 M KOH electrolyte within the potential range of 0–0.6 V. The analysis was done at various scan speeds from 10 mV s^{-1} to 150 mV s^{-1}. For all three materials, the current response rose with increasing scan speeds, suggesting that a diffusion-controlled process controlled the electrode kinetics. The CV curves were further utilised to determine the electrochemically active surface area (ECSA) of the applied catalysts. The CV curves at different scan rates were taken in the non-faradic region to obtain the double layer capacitance (C_{dl}) value, as both ECSA and C_{dl} values are proportional to each other. The C_{dl} values were calculated and are shown in Fig. 9(d). The GVS-2 sample showed the highest C_{dl} value of 5.72 mF cm^{-2} among the three samples, which indicates that it had the highest number of electrochemically active sites present among the samples. From the formula, ECSA = C_{dl}/C_s, C_s is specific capacitance, having a constant value of 0.04 mF cm^{-2} for metal electrodes in a KOH electrolyte.[56] The ECSA values were calculated for the three samples and were found to be approximately 143 cm^2 for the GVS-2 sample, 85 cm^2 for the GVS-1 sample, and 52 cm^2 for the VS sample, respectively. We clearly found from the calculations that the highest Gd-doped sample, GVS-2, had the highest electrochemically active surface area compared with the other samples.

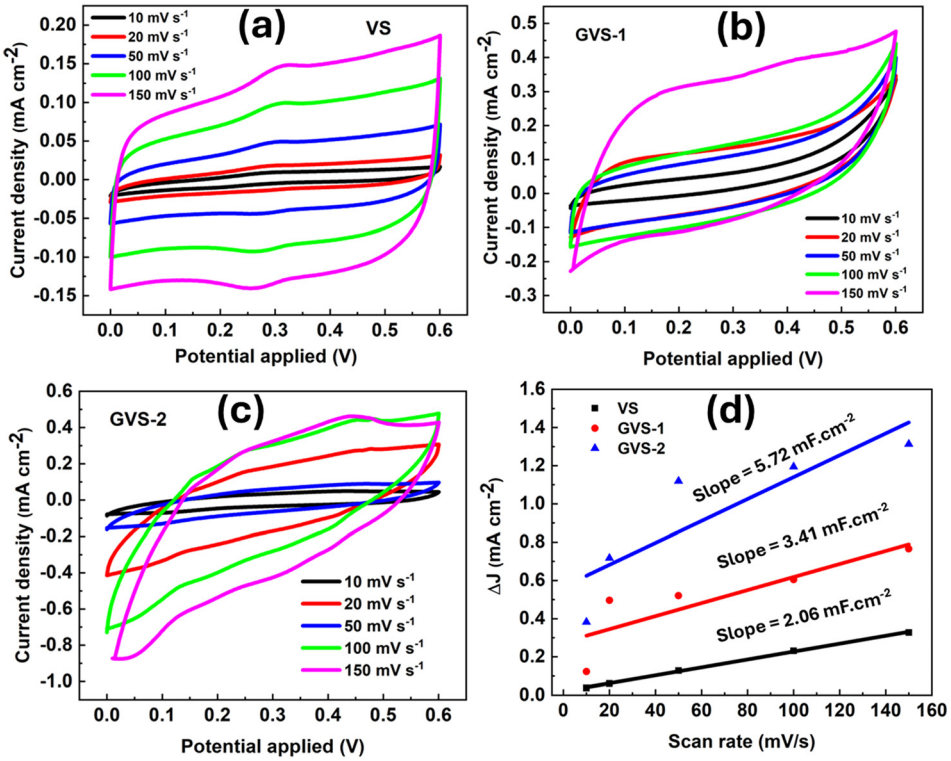

Fig. 9 CV curves of the (a) VS, (b) GVS-1, and (c) GVS-2 nanocomposites at various scan rates. (d) Calculation of the double layer capacitance (C_{dl}) values of the VS, GVS-1, and GVS-2 samples.

4. Conclusion

In summary, we prepared VSe_2 and Gd-doped VSe_2 nanocomposites through the hydrothermal method for use as HER catalysts. The synthesized nanocomposites were crystalline with a pure VSe_2 phase, according to the crystallographic analysis. As a result of the Gd doping, there was a peak shift towards lower angles. The optical study revealed that the bandgap varied between 2.6 to 3.6 eV for the synthesized samples and the bandgap increased as the degree of Gd doping increased. The synthesized samples had uniform nanoflower-like shapes that helped to increase the active surface area by increasing the number of exposed edges inside the sample. Consequently, the higher surface area increased HER catalytic activity. The GVS-2 sample with higher Gd doping exhibited an excellent HER performance. The GVS-2 sample had a lower onset potential of approximately 210 mV and a lower Tafel slope of approximately 60 mV per decade. The impedance study revealed that the GVS-2 sample had a low charge-transfer resistance of around 1.30 kΩ, which indicates that the sample had higher active edge sites compared to the other samples. Furthermore, the CV curves at different scan rates in the non-faradic region revealed that for all three materials that the current responses rose with increasing scan speeds, suggesting that a diffusion-controlled process controlled the electrode kinetics. The ECSA value was then calculated, and the GVS-2 sample showed the highest ECSA value, which agreed with its higher HER performance. From all the above-mentioned results, we can conclude that the higher Gd-doped VSe_2 sample works as an excellent electrocatalyst for HER performance.

Conflicts of interest

For this manuscript, there are no conflicts of interest among the authors.

Data availability

The data supporting this article have been included in the manuscript, which are available from the corresponding author. The data are plotted with the help of the Origin software. Analysis and quantification of images were performed using the ImageJ software.

Acknowledgements

The author, Dr. R. Naik, thanks the Science and Engineering Research Board (SERB), Govt. of India (CRG/2022/003084). He also thanks the central instrumentation facility of ICT-IOC for different experiments.

References

1 L. Chang, Z. Sun and Y. H. Hu, 1T Phase transition metal dichalcogenides for hydrogen evolution reaction, *Electrochem. Energy Rev.*, 2021, **4**, 194–218.

2 J. Wang, J. Liu, B. Zhang, X. Ji, K. Xu, C. Chen, L. Miao and J. Jiang, The mechanism of hydrogen adsorption on transition metal dichalcogenides as hydrogen evolution reaction catalyst, *Phys. Chem. Chem. Phys.*, 2017, **19**, 10125–10132.

3 D. Er, H. Ye, N. C. Frey, H. Kumar, J. Lou and V. B. Shenoy, Prediction of enhanced catalytic activity for hydrogen evolution reaction in janus transition metal dichalcogenides, *Nano Lett.*, 2018, **18**, 3943–3949.

4 Q. Lu, Y. Yu, Q. Ma, B. Chen and H. Zhang, 2D Transition-metal-dichalcogenide-nanosheet-based composites for photocatalytic and electrocatalytic hydrogen evolution reactions, *Adv. Mater.*, 2016, **28**, 1917–1933.

5 A. Mondal and A. Vomiero, 2D Transition metal dichalcogenides-based electrocatalysts for hydrogen evolution reaction, *Adv. Funct. Mater.*, 2022, **32**, 2208994.

6 D. Kong, J. J. Cha, H. Wang, H. R. Lee and Y. Cui, First-row transition metal dichalcogenide catalysts for hydrogen evolution reaction, *Energy Environ. Sci.*, 2013, **6**, 3553–3558.

7 J. Yang and H. S. Shin, Recent advances in layered transition metal dichalcogenides for hydrogen evolution reaction, *J. Mater. Chem. A*, 2014, **2**, 5979–5985.

8 W. Yu, J. Li, T. S. Herng, Z. Wang, X. Zhao, X. Chi, W. Fu, I. Abdelwahab, J. Zhou, J. Dan, Z. Chen, Z. Chen, Z. Li, J. Lu, S. J. Pennycook, Y. P. Feng, J. Ding and K. P. Loh, Chemically exfoliated VSe_2 monolayers with room-temperature ferromagnetism, *Adv. Mater.*, 2019, **31**, 1903779.

9 D. Voiry, M. Salehi, R. Silva, T. Fujita, M. Chen, T. Asefa, V. B. Shenoy, G. Eda and M. Chhowalla, Conducting MoS_2 nanosheets as catalysts for hydrogen evolution reaction, *Nano Lett.*, 2013, **13**, 6222–6227.

10 Z. Zhang, J. Niu, P. Yang, Y. Gong, Q. Ji, J. Shi, Q. Fang, S. Jiang, H. Li, X. Zhou, L. Gu, X. Wu and Y. Zhang, Van der waals epitaxial growth of 2D metallic vanadium diselenide single crystals and their extra-high electrical conductivity, *Adv. Mater.*, 2017, **29**, 1702359.

11 M. S. Dresselhaus and I. L. Thomas, Alternative energy technologies, *Nature*, 2001, **414**(6861), 332–337.

12 R. Ali, A. Shan, G. Saranya, X. Jian, A. Mahmood, N. Mahmood, M. Chen, Y. Yang and W. M. Lau, Bifunctional water-electrolysis-catalysts meeting band-diagram analysis: case study of "FeP" electrodes, *J. Mater. Chem. A*, 2020, **8**, 20021–20029.

13 J. Greeley, T. F. Jaramillo, J. Bonde, I. Chorkendorff and J. K. Norskov, Computational high-throughput screening of electrocatalytic materials for hydrogen evolution, *Nat. Mater.*, 2006, **511**(5), 909–913.

14 J. A. Turner, Sustainable hydrogen production, *Science*, 2004, **305**, 972–974.

15 S. Bai, C. Wang, M. Deng, M. Gong, Y. Bai, J. Jiang and Y. Xiong, Surface polarization matters: enhancing the hydrogen-evolution reaction by shrinking pt shells in Pt–Pd–graphene stack structures, *Angew. Chem., Int. Ed.*, 2014, **53**, 12120–12124.

16 E. Casado-Rivera, D. J. Volpe, L. Alden, C. Lind, C. Downie, T. Vázquez-Alvarez, A. C. D. Angelo, F. J. DiSalvo and H. D. Abruña, Electrocatalytic activity of ordered intermetallic phases for fuel cell applications, *J. Am. Chem. Soc.*, 2004, **126**, 4043–4049.

17 W. Yang and S. Chen, Recent progress in electrode fabrication for electrocatalytic hydrogen evolution reaction: A mini review, *Chem. Eng. J.*, 2020, **393**, 124726.

18 N. Mahmood, Y. Yao, J. W. Zhang, L. Pan, X. Zhang and J. J. Zou, Electrocatalysts for hydrogen evolution in alkaline electrolytes: mechanisms, challenges, and prospective solutions, *Adv. Sci.*, 2018, **5**, 1700464.

19 W. Zhao, B. Dong, Z. Guo, G. Su, R. Gao, W. Wang and L. Cao, Colloidal synthesis of VSe2 single-layer nanosheets as novel electrocatalysts for the hydrogen evolution reaction, *Chem. Commun.*, 2016, **52**, 9228–9231.

20 A. Parida, A. Devarajan and R. Naik, High-performance, fast-response photodetectors based on hydrothermally synthesized $V_{1-x}Mo_xSe_2$ nanosheets, *Dalton Trans.*, 2025, **54**, 1111–1126.

21 J. Yuan, J. Wu, W. J. Hardy, P. Loya, M. Lou, Y. Yang, S. Najmaei, M. Jiang, F. Qin, K. Keyshar, H. Ji, W. Gao, J. Bao, J. Kono, D. Natelson, P. M. Ajayan, J. Lou, J. Yuan, J. Wu, P. Loya, Y. Yang, S. Najmaei, M. Jiang, K. Keyshar, P. M. Ajayan, J. Lou, W. J. Hardy, H. Ji, D. Natelson, M. Lou, W. Gao, J. Kono, F. Qin and J. Bao, Facile synthesis of single crystal vanadium disulfi de nanosheets by chemical vapor deposition for efficient hydrogen evolution reaction, *Adv. Mater.*, 2015, **27**(37), 5605–5609.

22 X. Wang, J. Wang, B. Wei, N. Zhang, J. Xu, H. Miao, L. Liu, C. Su, Y. Li and Z. Wang, Plasma tailoring in WTe_2 nanosheets for efficiently boosting hydrogen evolution reaction, *J. Mater. Sci. Technol.*, 2021, **78**, 170–175.

23 Y. Yan, S. Xu, H. Li, N. C. S. Selvam, J. Y. Lee, H. Lee and P. J. Yoo, Perpendicularly anchored $ReSe_2$ nanoflakes on reduced graphene oxide support for highly efficient hydrogen evolution reactions, *Chem. Eng. J.*, 2021, **405**, 126728.

24 Y. A. Eshete, N. Ling, S. Kim, D. Kim, G. Hwang, S. Cho and H. Yang, Vertical heterophase for electrical, electrochemical, and mechanical manipulations of layered $MoTe_2$, *Adv. Funct. Mater.*, 2019, **29**, 1904504.

25 P. Zhuang, Y. Sun, P. Dong, W. Smith, Z. Sun, Y. Ge, Y. Pei, Z. Cao, P. M. Ajayan, J. Shen and M. Ye, Revisiting the role of active sites for hydrogen evolution reaction through precise defect adjusting, *Adv. Funct. Mater.*, 2019, **29**, 1901290.

26 V. Kuraganti, A. Jain, R. Bar-Ziv, A. Ramasubramaniam and M. Bar-Sadan, Manganese doping of $MoSe_2$ promotes active defect sites for hydrogen evolution, *ACS Appl. Mater. Interfaces*, 2019, **11**, 25155–25162.

27 C. Dai, Z. Zhou, C. Tian, Y. Li, C. Yang, X. Gao and X. Tian, Large-scale synthesis of graphene-like $MoSe_2$ nanosheets for efficient hydrogen evolution reaction, *J. Phys. Chem. C*, 2017, **121**, 1974–1981.

28 L. Lin, P. Sherrell, Y. Liu, W. Lei, S. Zhang, H. Zhang, G. G. Wallace and J. Chen, Engineered 2D transition metal dichalcogenides—A vision of viable hydrogen evolution reaction catalysis, *Adv. Energy Mater.*, 2020, **10**, 1903870.

29 Y. Li, H. Wang, L. Xie, Y. Liang, G. Hong and H. Dai, MoS_2 nanoparticles grown on graphene: An advanced catalyst for the hydrogen evolution reaction, *J. Am. Chem. Soc.*, 2011, **133**, 7296–7299.
30 W. Hua, H. H. Sun, F. Xu and J. G. Wang, A review and perspective on molybdenum-based electrocatalysts for hydrogen evolution reaction, *Rare Met.*, 2020, **39**, 335–351.
31 J. Kibsgaard, Z. Chen, B. N. Reinecke and T. F. Jaramillo, Engineering the surface structure of MoS_2 to preferentially expose active edge sites for electrocatalysis, *Nat. Mater.*, 2012, **11**, 963–969.
32 K. Zhang, Y. Li, S. Deng, S. Shen, Y. Zhang, G. Pan, Q. Xiong, Q. Liu, X. Xia, X. Wang and J. Tu, Molybdenum selenide electrocatalysts for electrochemical hydrogen evolution reaction, *ChemElectroChem*, 2019, **6**, 3530–3548.
33 S. Ramaraj, M. Sakthivel, S. M. Chen, B. S. Lou and K. C. Ho, Defect and additional active sites on the basal plane of manganese-doped molybdenum diselenide for effective enzyme immobilization: in vitro and in vivo real-time analyses of hydrogen peroxide sensing, *ACS Appl. Mater. Interfaces*, 2019, **11**, 7862–7871.
34 P. J. Gasper, Y. Lu, A. Y. Nikiforov, S. N. Basu, S. Gopalan and U. B. Pal, Detailed electrochemical performance and microstructural characterization of nickel – Yttria stabilized zirconia cermet anodes infiltrated with nickel, gadolinium doped ceria, and nickel – Gadolinium doped ceria nanoparticles, *J. Power Sources*, 2020, **447**, 227357.
35 T. ul Haq, S. A. Mansour, A. Munir and Y. Haik, Gold-supported gadolinium doped CoB amorphous sheet: a new benchmark electrocatalyst for water oxidation with high turnover frequency, *Adv. Funct. Mater.*, 2020, **30**, 1910309.
36 A. Parida, B. Dandasena, T. K. Mallik, S. Chinnaiyah and R. Naik, Optical nonlinearity of Gd-doped VSe_2 nanoflowers for photonic device applications, *Nanoscale Adv.*, 2025, **7**, 3281–3292.
37 W. Wang, X. Zhang, W. Wang, Y. Xue, D. Sheng, M. Xie and A. Xie, Synthesis of flowerlike vanadium diselenide microspheres for efficient electromagnetic wave absorption, *Nanotechnology*, 2024, **35**, 305704.
38 J. Yang, M. Gao, L. Yang, Y. Zhang, J. Lang, D. Wang, Y. Wang, H. Liu and H. Fan, Low-temperature growth and optical properties of Ce-doped ZnO nanorods, *Appl. Surf. Sci.*, 2008, **255**, 2646–2650.
39 A. Parida, S. K. Samal, S. Chinnaiah and R. Naik, SnS/MnSe Heterostructures for Enhanced Optoelectronics and Dielectric Applications, *Nanoscale Adv.*, 2024, **6**, 6365–6377.
40 M. Parishani, M. Nadafan and S. Akbarpoor, Enhancement of Third-Order Optical Nonlinearity of VSe_2 by Hybridizing with $CoSe_2$ as Flower-like Nanoparticles, *RSC Adv.*, 2024, **14**, 27741–27748.
41 T. G. Ulusoy Ghobadi, B. Patil, F. Karadas, A. K. Okyay and E. Yilmaz, Catalytic Properties of Vanadium Diselenide: A Comprehensive Study on Its Electrocatalytic Performance in Alkaline, Neutral, and Acidic Media, *ACS Omega*, 2017, **2**, 8319–8329.
42 X. Ren, X. Jing, L. Liu, L. Guo, M. Zhang and Y. Li, Easy Preparation of an MRI Contrast Agent with High Longitudinal Relaxivity Based on Gadolinium Ions-Loaded Graphene Oxide, *RSC Adv.*, 2014, **4**, 53987–53992.
43 H. Yang, T. Yang, H. Zhu, M. Zhang and M. Du, Synthesis of $MoSe_2$/Carbon Nanofibers Hybrid and Its Hydrogen Evolution Reaction Performance, *Chem. Lett.*, 2016, **45**, 69–71.
44 P. Makuła, M. Pacia and W. Macyk, How to correctly determine the band gap energy of modified semiconductor photocatalysts based on UV-Vis spectra, *J. Phys. Chem. Lett.*, 2018, **9**, 6814–6817.
45 S. Landi, I. R. Segundo, E. Freitas, M. Vasilevskiy, J. Carneiro and C. J. Tavares, Use and misuse of the Kubelka-Munk function to obtain the band gap energy from diffuse reflectance measurements, *Solid State Commun.*, 2022, **341**, 114573.
46 M. Yan, X. Pan, P. Wang, F. Chen, L. He, G. Jiang, J. Wang, J. Z. Liu, X. Xu, X. Liao, J. Yang and L. Mai, Field-Effect Tuned Adsorption Dynamics of VSe_2 Nanosheets for Enhanced Hydrogen Evolution Reaction, *Nano Lett.*, 2017, **17**, 4109–4115.
47 Y. Shi, Y. Zhou, D. R. Yang, W. X. Xu, C. Wang, F. Bin Wang, J. J. Xu, X. H. Xia and H. Y. Chen, Energy Level Engineering of MoS_2 by Transition-Metal Doping for Accelerating Hydrogen Evolution Reaction, *J. Am. Chem. Soc.*, 2017, **139**, 15479–15485.
48 H. Begum, M. N. Islam, S. Ben Aoun, J. A. Safwan, S. S. Shah, M. A. Aziz and M. A. Hasnat, Electrocatalytic reduction of nitrate ions in neutral medium at coinage metal-modified platinum electrodes, *Environ. Sci. Pollut. Res.*, 2023, **30**, 34904–34914.
49 B. E. Conway and B. V. Tilak, Interfacial processes involving electrocatalytic evolution and oxidation of H_2, and the role of chemisorbed H, *Electrochim. Acta*, 2002, **47**, 3571–3594.
50 X. Wang, Y. Chen, B. Zheng, F. Qi, J. He, P. Li and W. Zhang, Few-layered WSe_2 nanoflowers anchored on graphene nanosheets: a highly efficient and stable electrocatalyst for hydrogen evolution, *Electrochim. Acta*, 2016, **222**, 1293–1299.
51 S. Ben Aoun, Nanostructured carbon electrode modified with N-doped graphene quantum dots–chitosan nanocomposite: a sensitive electrochemical dopamine sensor, *R. Soc. Open Sci.*, 2017, **4**, 171199.
52 W. Argoubi, M. Saadaoui, S. Ben Aoun and N. Raouafi, Optimized design of a nanostructured SPCE-based multipurpose biosensing platform formed by ferrocene-tethered electrochemically-deposited cauliflower-shaped gold nanoparticles, *Beilstein J. Nanotechnol.*, 2015, **6187**(6), 1840–1852.
53 A. Mars, W. Argoubi, S. Ben Aoun and N. Raouafi, Induced conformational change on ferrocenyl-terminated alkyls and their application as transducers for label-free immunosensing of Alzheimer's disease biomarker, *RSC Adv.*, 2015, **6**, 2414–2421.
54 N. Tanjila, M. Ahsan, S. Ben Aoun, I. A. Siddiquey, S. S. Alam and M. A. Hasnat, An Electrochemical Approach to as(V) determination via an interaction with alizarin red s in aqueous medium, *J. Anal. Chem.*, 2021, **76**, 1449–1454.

55 P. C. Kumar, A. A. Nechikott, P. K. Nayak, D. Alagarasan and R. Naik, Superior Performance of 2D Layered Bimetallic Bismuth and Copper Oxytellurides for Supercapacitor applications, *ACS Appl. Energy Mater.*, 2024, **19**, 8478–8488.

56 C. C. L. McCrory, S. Jung, J. C. Peters and T. F. Jaramillo, Benchmarking heterogeneous electrocatalysts for the oxygen evolution reaction, *J. Am. Chem. Soc.*, 2013, **135**, 16977–16987.